Braz J Phys (2015) 45:308–313
DOI 10.1007/s13538-015-0323-1

SOCIEDADE BRASILEIRA DE FÍSICA

CONDENSED MATTER

# Effect of Aluminum Doping on the Nanocrystalline ZnS:$Al^{3+}$ Films Fabricated on Heavily-Doped *p*-type Si(100) Substrates by Chemical Bath Deposition Method

**He-Jie Zhu[1] · Yan Liang[2] · Xiao-Yong Gao[1] · Rui-Fang Guo[1] · Qiang-Min Ji[1]**

Received: 18 January 2015 / Published online: 21 April 2015


**Abstract** Intrinsic ZnS and aluminum-doped nanocrystalline ZnS (ZnS:$Al^{3+}$) films with zinc-blende structure were fabricated on heavily-doped *p*-type Si(100) substrates by chemical bath deposition method. Influence of aluminum doping on the microstructure, and photoluminescent and electrical properties of the films, were intensively investigated. The average crystallite size of the films varying in the range of about 9.0 ∼ 35.0 nm initially increases and then decreases with aluminum doping contents, indicating that the crystallization of the films are initially enhanced and then weakened. The incorporation of $Al^{3+}$ was confirmed from energy dispersive spectrometry and the induced microstrain in the films. Strong and stable visible emission band resulting from the defect-related light emission were observed for the intrinsic ZnS and ZnS:$Al^{3+}$ films at room temperature. The photoluminescence related to the aluminum can annihilate due to the self-absorption of ZnS:$Al^{3+}$ when the $Al^{3+}$ content surpasses certain value. The variation of the resistivity of the films that initially reduces and then increases is mainly caused by the partial substitute for $Zn^{2+}$ by $Al^{3+}$ as well as the enhanced crystallization, and by the enhanced crystal boundary scattering, respectively.

✉ Xiao-Yong Gao
xygao@zzu.edu.cn

[1] Key Laboratory of Material Physics of Ministry of Education, School of Physics and Engineering, Zhengzhou University, Zhengzhou 450052, China

[2] College of Information Science and Engineering, Henan University of Technology, Zhengzhou 450001, China

**Keywords** ZnS films · Chemical bath deposition · Optical properties · Aluminum doping

## 1 Introduction

In the last decade, much attention has been focused on the synthesis of group II–VI semiconductor materials due to their important applications in catalysis, optical devices, and so on. ZnS, an important semiconductor compound of the II–VI group, has attracted great attention due to its excellent physical properties and wide band gap energy of 3.68 eV at 300 K [1, 2]. ZnS films have potential applications in optoelectronics and film electroluminescent devices.

Many fabrication approaches have been employed to improve the electro-optical properties of intrinsic ZnS nanocrystals. Doping suitable dopant can effectively improve the performance of ZnS films. The ZnS films doped with copper show a decrease in the transmission and band gap energy, and a significant increase in resistivity [3]. The optical absorption spectra of the ZnS nanocrystals show a blue shift in the absorption edge with increasing Fe content [4, 5]. The electrical conductivity is found to be enhanced with the addition of Hg in host ZnS and the sample exhibits a variable hopping conduction mechanism [6]. Pathak et al. [7] used a chemical method to fabricate $Mn^{2+}$-doped ZnS nanoparticles passivated by acrylic acid, and they observed enhanced luminescence and $Mn^{2+}$-related yellow emission at 574 nm at room temperature.

There are a variety of methods that have been reported for fabricating intrinsic and doped ZnS films. Compared with other methods, chemical bath deposition (CBD) is economical, simple, and suitable for large-area deposition. CBD is also favorable to realize the doping of different dopants. Thus, in the present work, we tried to study the

microstructure, optical and electrical properties of the aluminum-doped ZnS ($ZnS:Al^{3+}$) films that were fabricated on heavily doped *p*-type Si(100) substrates in a weak acidic bath filled by zinc acetate ($Zn(CH_3COO)_2{\cdot}2H_2O$), aluminium chloride ($AlCl_3$), the complexing agent ethylenediamine (En), and thioacetamide (TAA) of analytical reagent grade. The aim is to analyze the effect of aluminum doping on the microstructure, optical, and electrical properties of $ZnS:Al^{3+}$ films. It is still crucial for the ZnS-based blue light-emitting devices to obtain high-quality ZnS film on heavily doped *p*-type Si(100) wafers with lower cost in order to facilitate the compatibility to traditional silicon integration processing. Heavily doped *p*-type Si (100) wafer was used as *p*-type layer of *n*-ZnS/*p*-Si heterojunction light-emitting devices.

## 2 Experiment

### 2.1 Synthesis of the Films

Intrinsic ZnS and $ZnS:Al^{3+}$ films were fabricated on heavily doped *p*-Si(100) substrates by CBD using different moles of $AlCl_3$. The silicon substrates were cleaned using conventional RCA processing and dried in the air for deposition. The used precursor solutions for the film deposition were prepared as zinc acetate dehydrate (1.00 M), thioacetamide (0.50 M), hydrochloric acid solution (2.00 M), complexing agent En (1.00 M), and $AlCl_3$ solution (0.20 M). Prior to the film deposition, 10 ml of zinc acetate solution, different mmol (0, 0.6, 1.0, 1.4, 1.8 mmol) of $AlCl_3$, and 10 ml of the En solutions were mixed in a beaker and stirred for several minutes to obtain a homogeneous milky white emulsion. HCl solution of 1 ml and TAA of 40 ml were then added to this white emulsion, and the mixture was stirred for several minutes. The pH value of the mixture was adjusted to 4 by addition of HCl solution. Then the clean Si substrates were placed in mixed solutions previously heated to 353 K in a baker oven and allowed to react at 353 K for 6.5 h. After deposition, the Si substrates were taken out of the reaction bath and washed for 15 min with de-ionized water, and dried in air. A yellow coating was coated on the substrate. For $ZnS:Al^{3+}$ films, the coating color was slightly pale yellow.

### 2.2 Characterization Techniques

X-ray diffractometer (X·pert Philips) with CuK$\alpha$ radiation and cold field scanning electron microscope (FE-SEM, JSM-6700) were used to extract the microstructure information (characterized by crystalline structure and surface morphology). Energy dispersive spectrometry (EDS) measurement was done to obtain the composition of the film. Fluorescent spectrometer (FluoroMax-4) was used to obtain the photoluminescence spectra of the films. The electrical resistivity of the films was measured using two-probe method while the conductivity type was determined by hot probe method. All measurements were conducted at room temperature.

## 3 Results and Discussion

### 3.1 Structural Properties

Figure 1 shows the X-ray diffraction patterns of the intrinsic ZnS and $ZnS:Al^{3+}$ nanocrystalline films with different mmol numbers of $AlCl_3$. Seen from Fig. 1, all the diffraction peaks of the films can be readily indexed to be the (111), (220), and (311) crystal planes of the cubic zinc-blende ZnS (JCPDF Card No. 03-065-0309). Intrinsic ZnS and $ZnS:Al^{3+}$ films have $< 111 >$ preferred orientation that is initially enhanced and then weakened with increasing the mmol number of $AlCl_3$. Similarly, the crystallization of the films is initially enhanced and then weakened as the mmol number of $AlCl_3$ increases. This result is quite close to the research done by Prathap et al. [8]. No impurity phase was observed, implying that only a small number of $Al^{3+}$ entered the ZnS lattice. This is confirmed by the EDS (Fig. 2). Figure 3 gives the calculated average crystallite size along $< 111 >$ orientation in terms of Debye-Scherrer equation [9]:

$$D = 0.94\lambda/(\beta \cos\theta), \tag{1}$$

where $D$ is the crystallite size, $\lambda$ is the X-ray wavelength ($\lambda$ = 0.15406 nm), $\beta$ is the full width at half maximum

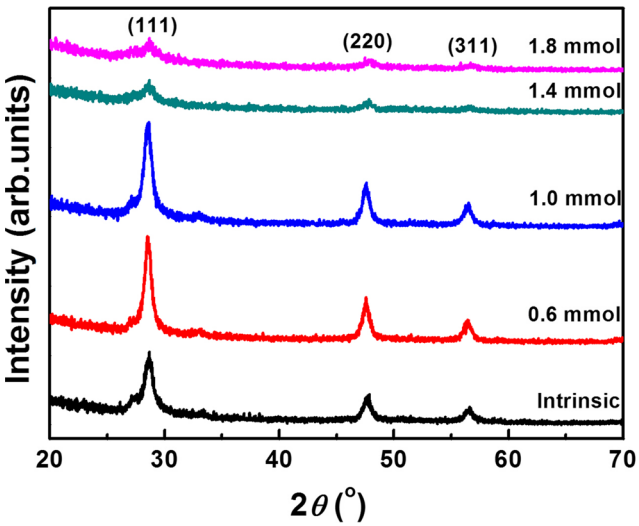


**Fig. 1** X-ray diffraction patterns of the intrinsic ZnS and $ZnS:Al^{3+}$ nanocrystalline films with different mmol numbers of $AlCl_3$ (color online)

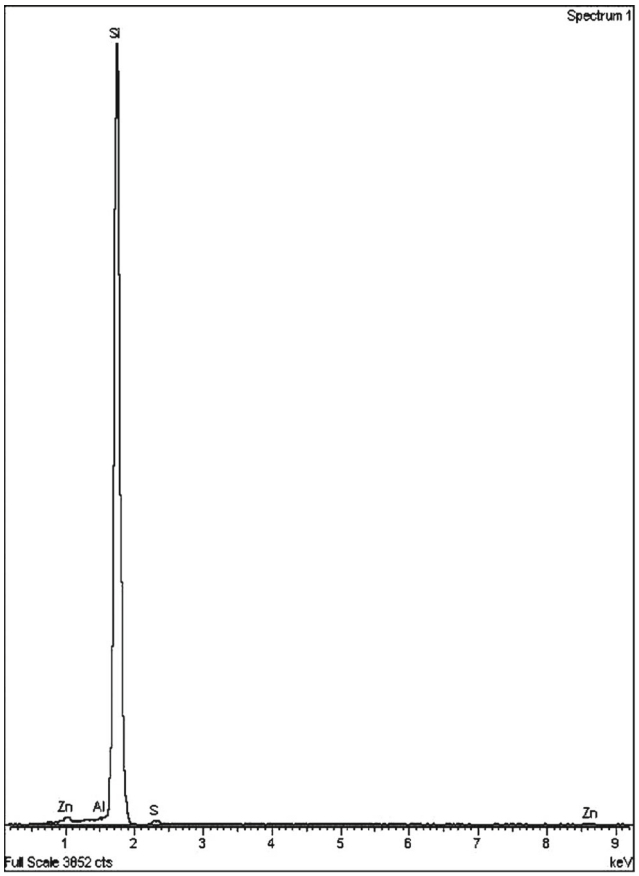


**Fig. 2** EDS pattern of the ZnS:$Al^{3+}$ nanocrystalline film with mmol number of $AlCl_3$ = 1.0 mmol

of diffraction peaks, and $\theta$ is the Bragg angle. The evaluated crystallite size varying in the range 9.0 $\sim$ 35.0 nm initially increases and then decreases with the mmol number of $AlCl_3$.

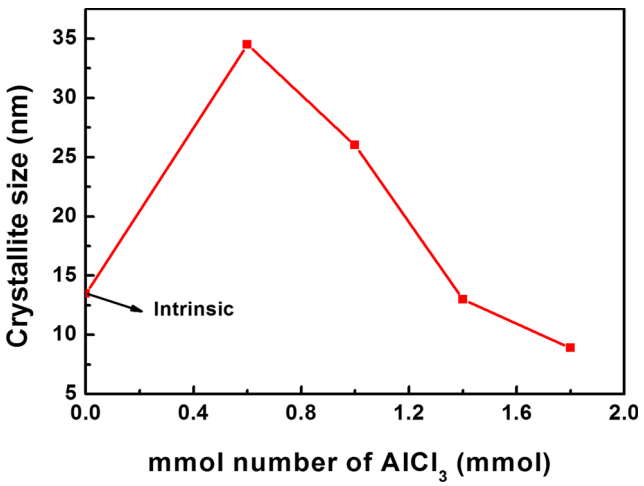


**Fig. 3** Calculated average crystallite size along < 111 > orientation in terms of Debye-Scherrer equation (color online)

It is noted in Fig. 1 that the diffraction peaks of ZnS:$Al^{3+}$films firstly narrow down and then broaden with mmol number of $AlCl_3$ value. The former is mainly due to the increasing crystallite size, while the latter is both due to the increased microstress and due to the decreasing average crystallite size. The change in crystallite size and microstress implies the change in lattice constant ($a$) that can be calculated using the Bragg equation [10]:

$$a = \lambda/(2\sin\theta)\left(h^2 + k^2 + l^2\right)^{1/2}, \tag{2}$$

where $\lambda$ is the X-ray wavelength ($\lambda$ = 0.15406 nm), $\theta$ is the Bragg angle, and ($hkl$) is the Miller index of crystal plane. The calculated lattice constant was 0.5379 nm for the intrinsic ZnS film, and 0.5421, 0.5400, 0.5332, and 0.5376 nm for the ZnS:$Al^{3+}$ films with mmol number of $AlCl_3$ of 0.6, 1.0, 1.4, and 1.8 mmol in sequence. This is mainly due to the partial substitute for the $Zn^{2+}$ (0.074 nm) by $Al^{3+}$ with smaller atomic radius (0.054 nm). The microstrain of the films along < 111 > orientation can be calculated according to the formula [11]:

$$\delta = (a_0 - a)/a_0, \tag{3}$$

where $a_0$ is the standard value of the crystal lattice constant of ZnS ($a_0$ = 0.5400 nm). The microstrain of the intrinsic ZnS film is $3.8\times10^{-3}$, and the microstrain of the ZnS:$Al^{3+}$ films with mmol number of $AlCl_3$ of 0.6, 1.0, 1.4, and 1.8 mmol are $-3.8\times10^{-3}$, 0, $1.2\times10^{-2}$, and $4.4\times10^{-3}$ in sequence. The ZnS:$Al^{3+}$ film with mmol number of $AlCl_3$ = 1.0 mmol has the smallest microstrain, indicating the film has the best crystallization. The result is in agreement with the X-ray diffraction results.

Figure 4 show the SEM micrographs of the intrinsic ZnS and ZnS:$Al^{3+}$ films with different mmol numbers of $AlCl_3$. Compared with the ZnS:$Al^{3+}$ films, the intrinsic ZnS film is more packed and denser. Random distribution of some small holes was observed on the surface of the ZnS:$Al^{3+}$ films. With increasing mmol number of $AlCl_3$, the surface of the films tends to be much sparser. This also confirms the entering of $Al^{3+}$ into the ZnS lattice. Besides, appearance of the clusters was observed in Fig. 4 with increasing the mmol number of $AlCl_3$. To some extend, cluster indicates the agglomeration of small crystallites, thus resulting into the production of more crystal boundaries. Enhancement of the crystal boundary scattering can increase the electrical resistivity.

### 3.2 Photouminescent Properties

Figure 5 shows the fluorescent photoluminecence spectra of the intrinsic ZnS and ZnS:$Al^{3+}$ films with different mmol numbers of $AlCl_3$. The excitation wavelength was 310 nm.

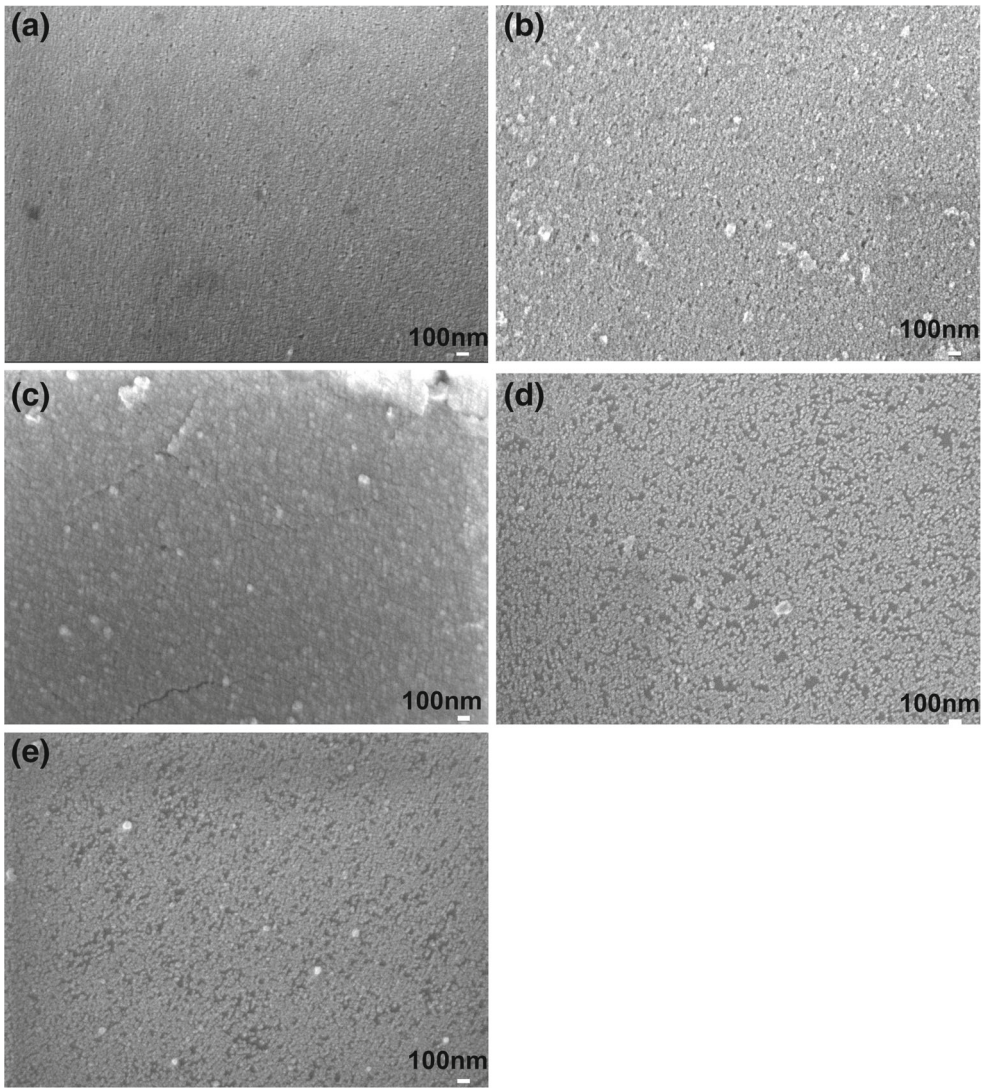


**Fig. 4** SEM micrographs of the **a** intrinsic ZnS film and ZnS:$Al^{3+}$ films with mmol number of $AlCl_3$ of **b** 0.6 mmol, **c** 1.0 mmol, **d** 1.4 mmol, and **e** 1.8 mmol

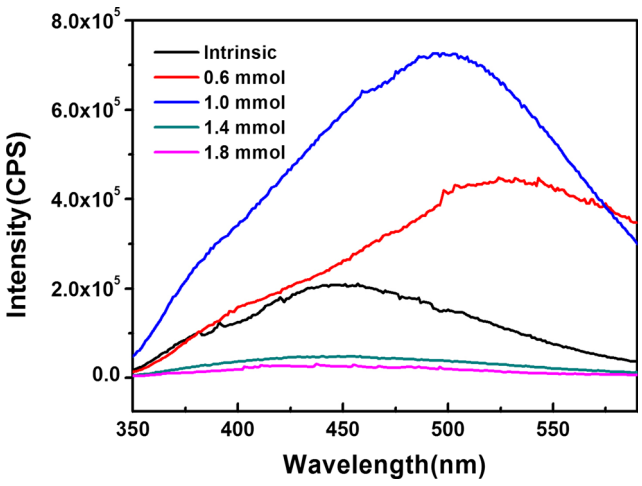


**Fig. 5** Photoluminecence spectra of the intrinsic and aluminum-doped ZnS films using different mmol numbers of $AlCl_3$ (color online)

All the films show a wide visible emission band. The emission intensity of the ZnS:$Al^{3+}$ films is initially enlarged and then sharply reduced with increasing the mmol number of $AlCl_3$. The emission intensity reaches the maximum at mmol number of $AlCl_3$ = 1.0 mmol. The change in emission intensity of the films is closely related to the change in the crystallization and defect contents of the films. Figure 6 gives the visible emission bands of the intrinsic ZnS and ZnS:$Al^{3+}$ films with different mmol numbers of $AlCl_3$. Karar et al. [12] reported that the photoluminecent central peak near 450 nm was attributed to native acceptor levels of ZnS film (i.e., S defects). Seen from Fig. 6, the photoluminescent central peak was located near 450 nm for the intrinsic ZnS film and ZnS:$Al^{3+}$ films with mmol number of $AlCl_3$ = 1.4 and 1.8 mmol. On the contrary, the photoluminescent central peak of the ZnS:$Al^{3+}$ films with mmol number of $AlCl_3$ = 0.6 and 1.0 mmol clearly

deviates away 450 nm. The photoluminescent central peak located near 450 nm is attributed to the native S acceptor defects. On the contrary to the ZnS film with mmol number of $AlCl_3$ = 0.6 and 1.0 mmol, the ZnS films at mmol number of $AlCl_3$ = 1.4 and 1.8 mmol do not show the photoluminescence peak related to the aluminum donor. Why? This may be attributed to the fact that additional $Al^{3+}$ can stack at the crystal boundary when $Al^{3+}$ content (i.e., mmol number of $AlCl_3$) surpasses certain value. The stacking of additional $Al^{3+}$ at the crystal boundary can induce the increased defects that may annihilate the $Al^{3+}$-related photoluminescence. The annihilation may arise from the self-absorption of ZnS:$Al^{3+}$. In order to make the photoluminescent mechanism clear, the wide visible emission bands of the ZnS:$Al^{3+}$ films with mmol number of $AlCl_3$ = 0.6, 1.0 mmol were decomposed into two photoluminescent peaks as seen in Fig. 6b, c. The two luminescent peaks may be both related to the defect levels of the films. The ratio of the integrated intensities of the two luminescent peaks sharply increases, implying that the the photoluminescence related to native S acceptor dopant increases with the mmol number of $AlCl_3$. The photoluminescent peak centred near 450 and 517 nm may be attributed to the native S acceptor dopant and Al donor dopant. The energy level diagram of the ZnS:$Al^{3+}$ film is shown in Fig. 7, where $V_S^*$ and $V_{Al}^*$ were the S acceptor level and Al donor level.

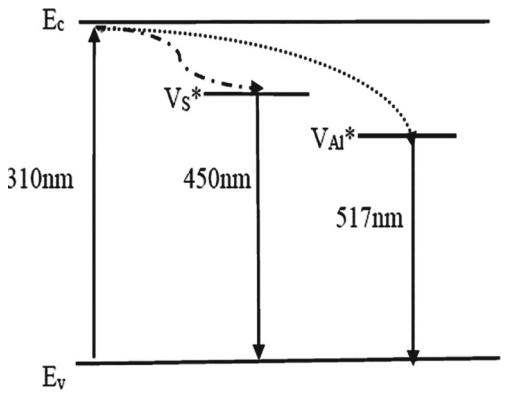


**Fig. 7** Energy level diagram of the ZnS:$Al^{3+}$ film

When irradiated by the 310-nm short-wavelength light, the electron at valence band edge is first excited to conduction band. The electron relaxation can make the electron indirectly transit to defect level. The electron transition from defect level to valence band is responsible for the visible

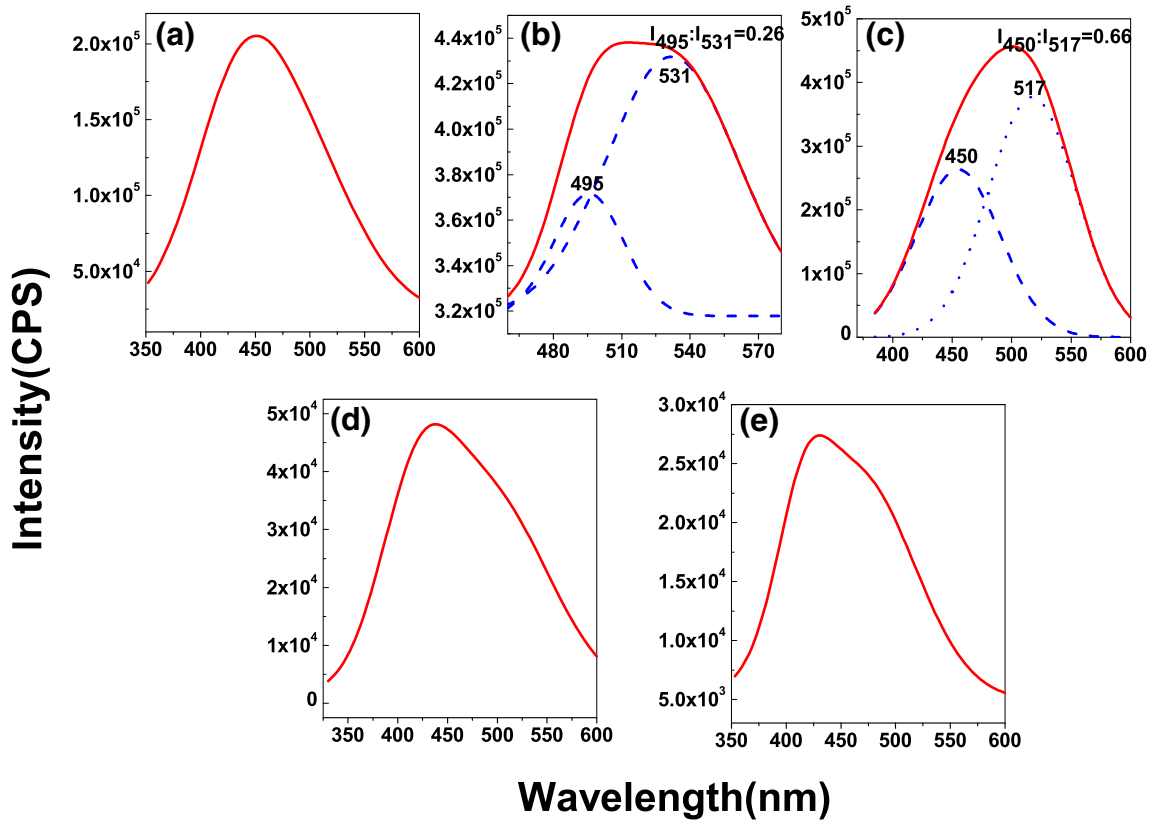


**Fig. 6** Visible emission band of the **a** intrinsic ZnS and ZnS:$Al^{3+}$ films with mmol numbers of $AlCl_3$ of **b** 0.6 mmol, **c** 1.0 mmol, **d** 1.4 mmol, and **e** 1.8 mmol. The ratio of the integrated intensity of the two photoluminescent peaks was also shown (color online)

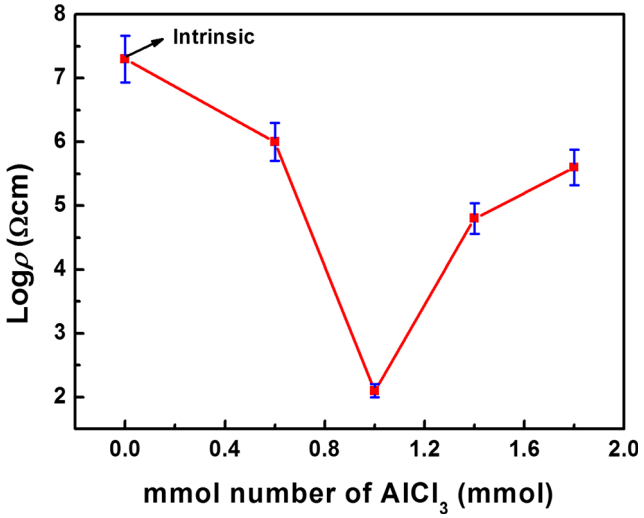


**Fig. 8** Electrical resistivity of the intrinsic ZnS and ZnS:$Al^{3+}$ films with different mmol number of $AlCl_3$ (color online)

luminescence. For the ZnS:$Al^{3+}$ film, the visible luminescence related to the S and Al defect seemingly occur simultaneously. However, when the $Al^{3+}$ content surpasses the certain value, the $Al^{3+}$ ions stacking at the crystal boundaries may result into the annihilation of the photoluminescence related to $Al^{3+}$ that may be due to the self-absorption of the ZnS:$Al^{3+}$ film.

### 3.3 Electrical Properties

The hot probe test indicates that the intrinsic ZnS and ZnS:$Al^{3+}$ films belong to *n*-conductivity type. The resistivity of the films strongly depends on the mmol number of $AlCl_3$ (i.e., the $Al^{3+}$ content in the films) as shown in Fig. 8. The electrical resistivity of the intrinsic ZnS film is $1.5\times10^7\Omega$ cm, which decreases to $4.2\times10^2\Omega$ cm at mmol number of $AlCl_3$ = 1.0 mmol and then increases with the mmol number of $AlCl_3$. The initial decrease of the resistivity with mmol number of $AlCl_3$ is mainly related to the partial substitute for $Zn^{2+}$ by $Al^{3+}$ that increases the free carrier content. Besides, enhanced crystallization of the films can improve the mobility of the free carriers, which also results into the decreased resistivity. The further increase in the resistivity with mmol number of $AlCl_3$ is mainly due to the enhanced crystal boundary scattering that is both due to the increasing crystal boundaries from the decreasing crystallite size and the agglomeration of small crystallites, and to the accumulation of the excessive $Al^{3+}$ at the crystal boundaries [13].

## 4 Conclusions

Intrinsic ZnS and ZnS:$Al^{3+}$ films with zinc-blende structure were fabricated on heavily doped *p*-type Si(100) substrates by CBD method. The crystallization and the intensity of the visible emission band of the films are initially enhanced and then weakened with mmol number of $AlCl_3$. The enhanced crystallization is mainly responsible for the initial increased emission intensity of the films. The partial substitution for $Zn^{2+}$ by $Al^{3+}$ mainly results into the initial decreased resistivity besides the enhanced crystallization. The further increase in the resistivity with mmol number of $AlCl_3$ is mainly due to the enhanced crystal boundary scattering that is both due to the increasing crystal boundaries from the decreasing crystallite size and the agglomeration of small crystallites, and to the accumulation of the excessive $Al^{3+}$ at the crystal boundaries. The wide visible emission related to the S acceptor dopant and Al donor dopant is initially enhanced and then weakened. The photoluminescent central peak near 450 and 517 nm is attributed to the native S acceptor dopant and to the Al donor dopant, respectively. The stacking of additional $Al^{3+}$ at the crystal boundary can annihilate the Al-related photoluminescence when the mmol number of $AlCl_3$ surpasses the certain value, which may be due to the self-absorption of the ZnS:$Al^{3+}$ film.

**Acknowledgments** We are grateful for the supports from the National Natural Science Foundation of China (Grant No. 60807001), the Foundation of Young Key Teachers from Univerisity of Henan Province (Grant No. 2011GGJS-008), and the Foundation of Henan Educational Committee (Grant No. 2010A140017).

## References

1. H. Soni, M. Chawda, D. Bodas, Mater. Lett. **63**, 767 (2009)
2. F. Gode, C. Gümüs, M. Zor, J. Crystal Growth **299**, 136 (2007)
3. Ö. Mustafa, B. Metin, A.N. Yazici, V.E. Kafadar, T. Hseyin, Physica B **381**, 40 (2006)
4. S. Sambasivam, B.K. Reddy, A. Divya, N. Madhusudhana Rao, C.K. Jayasankar, B. Sreedhar, Phys. Lett. A **373**, 1465 (2009)
5. C.M. Huang, L.C. Chen, G.T. Pan, C.K. Yang, W.S. Chang, K.W. Cheng, Mater. Chem. Phys. **117**, 156 (2009)
6. A.R. Pawar, D.R. Kendre, V.B. Pujari, International Journal of Advances in Electrical and Electronics Engineering **2**, 68 (2013)
7. C.S. Pathak, M.K. Mandal, Chalcogenide Lett. **8**, 147 (2011)
8. P. Prathap, N. Revathi, Y.P.V. Subbaiah, K.T.R. Reddy, R.W. Miles, Solid State Sci. **11**, 224 (2009)
9. B.D. Cullity, *Elements of X-ray Diffraction*, 2nd edn. (Addison-Wesley publishing co. Inc, London, 1978), p. 327
10. W.L. Bond, Acta Crystallogr **13**, 814 (1960)
11. N. Choudhury, B.K. Sarma, Bull. Mater. Sci. **32**, 43 (2009)
12. N. Karar, F. Singh, B.R. Mehta, J. Appl. Phys. **95**, 656 (2004)
13. M.J. Alam, D.C. Cameron, J. Vac. Sci. Technol. A **19**, 1642 (2001)